Magnetoelastic resonance as a probe for exchange springs at antiferromagnet-ferromagnet interfaces

K. M. Seemann, O. Gomonay, Y. Mokrousov, A. Hörner, S. Valencia, P. Klamser, F. Kronast,
A. Erb, A. T. Hindmarch, A. Wixforth, C. H. Marrows, and P. Fischer

Magneto-elastic resonance as a probe for exchange springs at antiferromagnet-ferromagnet interfaces

K. M. Seemann,[1, 2, *] O. Gomonay,[3] Y. Mokrousov,[3, 4] A. Hörner,[5] S. Valencia,[6] P. Klamser,[6]
F. Kronast,[6] A. Erb,[7] A. T. Hindmarch,[8, 2] A. Wixforth,[5] C. H. Marrows,[2] and P. Fischer[9, 10]

[1]*Université de Lorraine, CNRS, IJL, F-54000 Nancy, France*
[2]*School of Physics and Astronomy, University of Leeds, Leeds, LS2 9JT, United Kingdom*
[3]*Institut für Physik, Johannes Gutenberg Universität Mainz, D-55099 Mainz, Germany*
[4]*Peter Grünberg Institut and Institute for Advanced Simulation,*
Forschungszentrum Jülich and JARA, D-52425 Jülich, Germany
[5]*Lehrstuhl für Experimentalphysik I and Augsburg Center for Innovative Technologies, ACIT, D-86159 Augsburg, Germany*
[6]*Helmholtz-Zentrum Berlin für Materialien und Energie,*
Albert-Einstein-Strasse 15, D-12489 Berlin, Germany
[7]*Walther Meissner Institut für Tieftemperaturforschung,*
Bayerische Akademie der Wissenschaften, Walther-Meissner-Str. 8, D-85748 Garching, Germany
[8]*Department of Physics, Durham University, Durham DH1 3LE, United Kingdom*
[9]*Materials Sciences Division, Lawrence Berkeley National Laboratory, Berkeley California 94720, USA*
[10]*Physics Department, University of California Santa Cruz, Santa Cruz 94056, California, USA*
(Dated: March 31, 2022)

In prototype ferromagnet-antiferromagnet interfaces we demonstrate that surface acoustic waves can be used to identify complex magnetic phases arising upon evolution of exchange springs in an applied field. Applying sub-GHz surface acoustic waves to study the domain structure of the ferromagnetic layer in exchange-biased bilayers of $Ir_{20}Mn_{80}$-$Co_{60}Fe_{20}B_{20}$, we are able to associate the magneto-elastic resonance with the presence of the exchange spin-spirals in both, the ferromagnetic and antiferromagnetic layer. Our findings offer a complementary, integrative insight into emergent magnetic materials for applications of non-collinear spin textures in view of low energy-consumption spintronic devices.

Keywords: Spin spirals, exchange bias, surface acoustic waves, XMCD-PEEM, IrMn, CoFeB, antiferromagnet-ferromagnet interface

An interplay between elastic properties of matter with magnetism has been a realm of strong interest for a long time, motivated both by practical aspects but also from the perspective of understanding the coupling between macroscopic structural properties and most fundamental quantum effects [1]. The magneto-elastic interaction of so-called surface acoustic waves (SAWs) [2, 3] within single-layer magnetic thin films deposited on-chip and their acousto-magnetic resonant attenuation in magnetic materials is a phenomenon that has received considerable attention in the past decades, owing to the uniqueness of the insights into magnetic and structural properties of the system that SAW attenuation can provide [4–6]. Measuring the attenuation of SAW amplitude as a function of the external magnetic field in different geometries is an effective tool to probe equilibrium magnetic structure [3]. Moreover, SAW-induced magnetic dynamics, such as domain wall motion [7] or ferromagnetic resonance [3], provide information about stability ranges of different magnetic phases and orientation transitions induced by an external magnetic field.

Very recently, the generation of magneto-acoustic modulations by launching surface acoustic waves on piezo-electric single-crystal substrates coated by magnetic thin films of Fe, Co and Ni was achieved, simultaneously being imaged using monochromatized circularly polarized synchrotron light and x-ray magnetic circular dichroism pho-toemission electron microscopy (XMCD-PEEM) [3, 8–10]. While the behavior of SAWs in such simple magnetic materials is relatively well understood, the interplay of SAWs with more complex magnetic structures presents a real challenge. A classical example of such complex magnetic order is found in ferromagnetic thin films that are exchange coupled to antiferromagnets or hard magnetic ferromagnets [11] that have been reported to show rich phases of non-collinear structures in magnetization similar to the helical magnetic structures and spin spirals found for example in exchange spring magnets, domain walls [12] and the magnetic vortices observed in nano-discs [13, 14]. In such systems, understanding of the SAW spectra can provide a unique means for accessing the details of magnetic phase transitions, not accessible with other techniques.

In this work we demonstrate that the interaction of SAWs with complex magnetism at the interfaces of ferromagnets and antiferromagnets can be reliably used to probe the main features in the intricate magnetic phase evolution of this prototype system arising in response to an external magnetic field. By combining sub-GHz SAW damping measurements based on a vector-network-analyzer (VNA) with high resolution XMCD-PEEM microscopy and with superconducting-quantum-interference-device vibrating-sample-magnetometry (SQUID-VSM), we investigate the
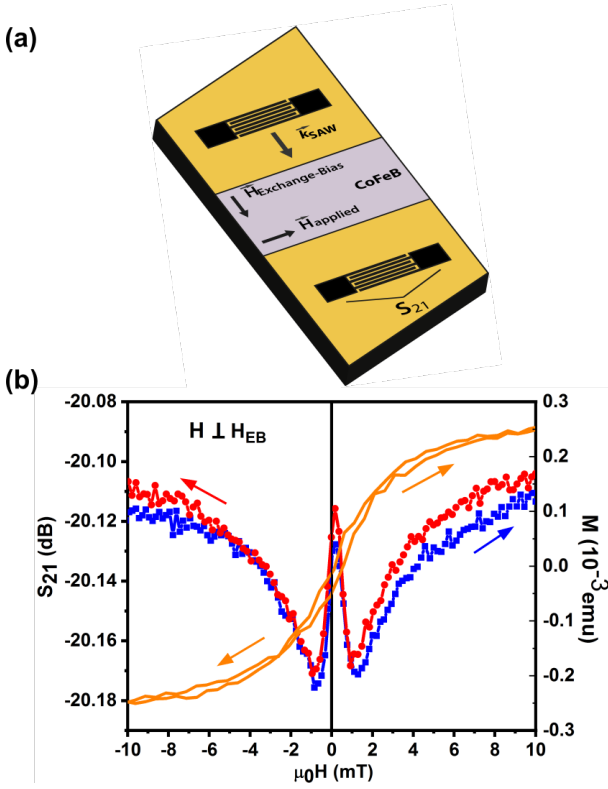
Figure 1. (Color online) Scheme of the on-chip SAW damping experiment (a) together with the interdigital transducers to launch SAWs. The wave vector $\mathbf{k}_{SAW}$ of the longitudinal SAW is parallel to the direction of the exchange bias field $\mathbf{H}_{EB}$. (b) The damping amplitude S_{21} (SAW power $P_{SAW} = 0.8$ mW) The field applied in-plane and perpendicular to the direction of the exchange bias field. The hysteretic magnetization curve for this geometry is shown in orange.

acousto-magnetic damping of surface acoustic waves within an exchange-biased polycrystalline $Co_{60}Fe_{20}B_{20}$ thin film. From an analysis of experimental data supported by microscopic theory model we show that sub-GHz SAW prove to be very sensitive to the spin textures in an exchange-biased antiferromagnet-ferromagnet heterostructure, which exhibits exchange spring spin spirals as a function of an externally applied field. This method may play an important role for novel magnetic devices on the basis of magneto-elastic effects analogous to ultrafast magnetization dynamics.

SURFACE ACOUSTIC WAVE EXPERIMENTS

In the following we describe details of the surface acoustic wave experiments applied in this work. The attenuation of SAWs by magneto-elastic coupling and spin wave excitations prove advantageous in studying non-colliniear magnetic spin textures otherwise non-trivial to observe experimentally.

As probe we used Rayleigh-mode SAWs generated on single-crystal piezoelectric lithium niobate substrates ($LiNbO_3$, rot. 128 y cut), tapered substrate edges served to prevent SAW back-reflection resulting in interference effects undesired in this experiment.

The exchange-biased CoFeB thin film of in-plane magnetization was deposited by magnetron sputtering in zero field at room temperature on-top of a tri-layer comprising a tantalum adhesion layer of thickness 2 nm was followed by 5 nm of permalloy $Ni_{20}Fe_{80}$ base layer to initiate antiferromagnetic ordering of the 20 nm thick $Ir_{20}Mn_{80}$. The stack of four layers yields an effective exchange-bias field of $\mu_0 H_{EB} \approx 3$ mT for the 20 nm thick amorphous $Co_{60}Fe_{20}B_{20}$ ferromagnetic thin film [15], [19]. The thin layer of permalloy is subject to an exchange bias from the IrMn layer, however with approximately 15 mT much larger than the main ferromagnet CoFeB, also contributing only a much lower magnetic moment at a thickness ratio $t(Co_{60}Fe_{20}B_{20})$ /$t(Ni_{20}Fe_{80})$ of 4/1.

The Rayleigh-mode surface acoustic waves were launched by interdigitated transducers deposited directly onto the lithium niobate substrates by evaporating 5 nm of a titanium adhesion layer and 20 nm of gold into microresist patterns structured by optical lithography and a subsequent lift-off technique. The lithographically defined SAW wavelength was $\lambda \approx 30$ μm. A schematic of the sample layout is shown in Fig. 1(a).

The damping of the sub-GHz SAW due to oscillations in non-collinear spin textures within the magnetic domains has a strong dependence on the magnetic field applied in-plane. A stack of magnetic thin films consisting of $Co_{60}Fe_{20}B_{20}$ ferromagnet exchange-coupled to an antiferromagnetic $Ir_{20}Mn_{80}$ (IrMn) base layer [16–18] generates in zero applied field a net magnetization with direction parallel to the exchange bias field of the antiferromagnet.

The on-chip damping measurements were performed using a vector network analyzer (VNA), where the high frequency signal supplied by the VNA is fed into IDT_1. For the measurement of the SAW transmission S_{21} the detector port of the VNA picks up the transmitted signal from IDT_2 measured in relation to the original input signal given in logarithmic relative units of decibel dB. The pulsed signal generation was combined with a time-gated detection to prevent parasitic effects. The inverse Fourier transform of the measurement is employed to gain the time-gated signal and a Fourier transform back to the frequency domain results yields S_{21}. The Kramers–Kronig relations are the basis for relating the phase velocity of the SAW to $\Delta S_{21} = \frac{b_2}{a_1}$ [22], where b_2 denotes the wave emitted and a_1 represents the incoming signal, see also schematic in Fig. 1 (a).

An incident SAW power of $P_{SAW} = -20$ dB_m equivalent to 10 μW) was used and increasing the SAW power up to $P_{SAW} = 10$ dB_m (equivalent to 10 mW) did not alter the recorded characteristic SAW attenuation pa-
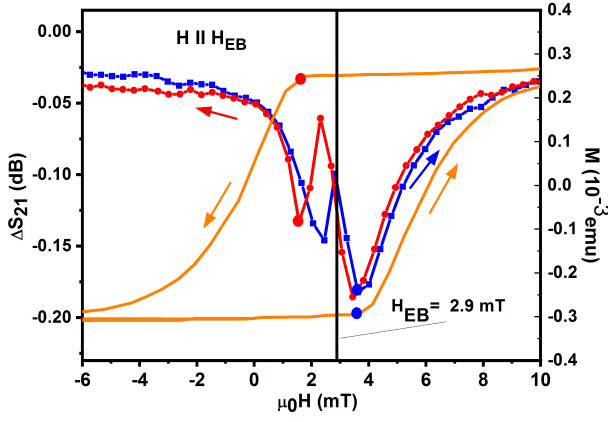
Figure 2. (Color online) The field dependence of SAW damping ΔS_{21} corrected for the background signal at high field to show the scale of the damping amplitude (blue squares and red circles, $\Delta S_{21} \approx -0.15$ dB at a SAW power of $P_{\mathrm{SAW}} = 10$ μW) along with the magnetization curve $M(H)$ (solid orange line). Large dots mark the stability ranges of $\mathbf{M} \uparrow\uparrow \mathbf{H}_{\mathrm{EB}}$ (large red dots) and $\mathbf{M} \downarrow\uparrow \mathbf{H}_{\mathrm{EB}}$ (large blue dots) states. Arrows show the direction of the field sweep. Both $M(H)$ and $\Delta S_{21}(H)$ loops show the exchange-bias shift by $\mu_0 H_{\mathrm{EB}}=2.9$ mT and the correlation between SAW peaks and domain formation (dots).

rameter ΔS$_{21}$. Hence, in this power regime, SAW-driven switching of magnetization as demonstrated in the work described by Davis et al. [21] can safely be ruled out.

In our experiments, on-chip generated SAWs at a higher harmonic frequency of $f_{\mathrm{SAW}} = 593$ MHz, advantageous in terms of signal-to-noise ratio, were transmitted and received from a pair of interdigital transducers patterned onto a single-crystal piezo-electric lithium niobate substrate [see Fig. 3(a)] and as such used to probe the magnetic state of the heterostructure. The SAW transmission parameter S_{21} is extracted from a change in SAW phase velocity following standard pulsed source Fourier transform measurements [22]. We measured the field-dependence of S_{21} during the sweep forward and backward from the saturation value using two geometries with the in-plane magnetic field $\mathbf{H}$ either perpendicular or parallel to the direction of the exchange bias field $\mathbf{H}_{\mathrm{EB}}$. The results of the measurements are illustrated in Figs. 3 (b) and Fig. 2 in combination with the magnetization loops $M(H)$ obtained by SQUID-VSM measured in the same geometry.

In the case of $\mathbf{H} \perp \mathbf{H}_{\mathrm{EB}}$ [Fig. 3(b)], the magnetization hysteresis loop is centered at $H = 0$ displaying critical fields of $\mu_0 H_{\mathrm{lc}} = -\mu_0 H_{\mathrm{rc}} \approx 0.95$ mT at which the switching of the magnetization begins. The SAW signal shows a similar behaviour with the peaks located at $H = H_{\mathrm{lc,rc}}$. We interpret the SAW signal within the $H_{\mathrm{lc}} \leq H \leq H_{\mathrm{rc}}$ interval originating from the spacial magnetic oscillations in a multidomain state of a ferromagnetic layer. More-

over, each maximum of damping in the measured SAW signal, exhibited as a dip in the experimental data of Fig. 1 (a) and 2, indicates the points of field-induced nucleation/disappearing of the metastable states ($\mathbf{M} \uparrow\uparrow \mathbf{H}_{\mathrm{EB}}$ (large red dots in Fig. 2) and $\mathbf{M} \downarrow\uparrow \mathbf{H}_{\mathrm{EB}}$ (large blue dots in Fig. 2)). We observe a similar correlation between the position of maximal SAW damping and the critical fields $\mu H_{\mathrm{lc}} \approx 1.8$ mT and $\mu H_{\mathrm{rc}} = 3.8$ mT for the parallel alignment of the external and the exchange bias fields $\mathbf{H}\|\mathbf{H}_{\mathrm{EB}}$ (Fig. 2). However, in this case both hysteretic loop and SAW signal exhibit an expected shift by $\mu H_{\mathrm{EB}} = 2.9$ mT.

MAGNETIC IMAGING BY XMCD-PEEM

To elucidate the link between the SAW signal and domain structure the local magnetization of the exchange-biased magnetic thin film was investigated by high-resolution magnetic imaging based on x-ray magnetic circular dichroism photoemission electron microscopy (XMCD-PEEM). The images were taken by the SPEEM instrument of the UE49-PGM microfocus beam line of the BESSY II facility [23, 24]. In order to trace the rotation of the net magnetization in the external magnetic field we used the magnetic domain contrast as a pointer. These domains, with an average width of approximately 300 nm, are stabilized due to the exchange bias field and can be imaged by XMCD-PEEM.

The insets in Fig. 3 (a) and Fig. 3 (b) display XMCD-PEEM images of the $Co_{60}Fe_{20}B_{20}$ magnetization for six different values of the in-plane magnetic field $\mathbf{H} \perp \mathbf{H}_{\mathrm{EB}}$, along with the field dependence of the SAW amplitude damping parameter ΔS_{21}. The $Co_{60}Fe_{20}B_{20}$ shows magnetic contrast arising from nano-width magnetic domains in zero field, the net magnetization follows the exchange bias direction. The magnetic contrast due to magnetic domains vanishes at $\mu H \approx 1$ mT which coincides with the critical field μH_{rc} and maximum in SAW signal, see Fig. 1 (b). Further increasing the magnetic field, the magnetization rotates gradually towards the field direction until it reaches a parallel alignment to the external field at $\mu H = 16$ mT as shown in Fig. 3 (a) and in more detail in Fig. 3 (b), wherein a map of arrows illustrates the local magnetization.

We observe a broadening of the XMCD signal (photoelectron intensity asymmetry ratio from left versus right circularly polarized incident light) for the magnetic domain state at 1 mT, which is attributed to a relaxation of the CoFeB and its spin texture. The XMCD signal was recorded at the Co-L$_3$ energy and originates from the escape depth of approximately 5 nm of the photoelectrons excited within the ferromagnet by monochromatized circularly polarized soft x-rays. The gradual rotation of the CoFeB thin film upon increasing the magnetic field applied perpendicular to the established exchange bias field is accompanied by a narrowed histogram of the field de-
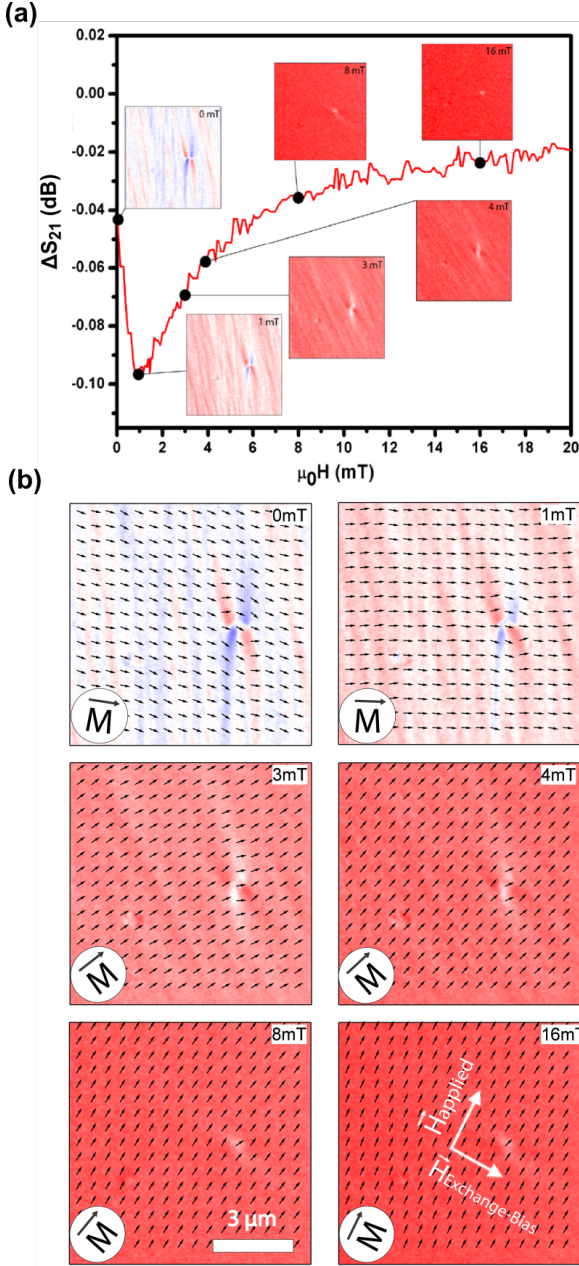
(a)

(b)

Figure 3. (Color online) (a) SAW damping ΔS_{21} vs. applied magnetic field together with XMCD-PEEM images (b) of the field dependent magnetic state of CoFeB illustrate the magnetic domains. The circles in the lower left corner of each image represents the orientation of the net magnetization in the CoFeB thin film. Red colour marks the fully aligned ferromagnetic layer along the external field, while blue colour indicates a local deviation of magnetic spins in zero field and the matrix of arrows maps the local direction of magnetization at the surface of the ferromagnet.

pendent XMCD signal shown in Fig. 4 (a). The CoFeB is fully aligned at 6 mT, which is also exemplified in the inset to Fig. 4 (a) showing the angle between the CoFeB magnetization and the exchange bias field. Addition-

ally, the FWHM values of the field dependent XMCD histogramms, obtained from the experimental XMCD-PEEM images as shown in Fig. 4 (b) as a function of the magnetic field applied perpendicular to the exchange bias field, reveal a maximum at 1 mT matching the SAW damping characteristics in this geometry well. The consecutively decreasing FWHM values for larger applied fields also follows a very similar trend to the SAW damping illustrated in Fig. 3 (a) above.

The correlation between SAW signal and the domain structure is corroborated by an analysis of the XMCD-PEEM images and the determined full width at half maximum (FWHM) and position of XMCD maxima as a function of the magnetic field (see Fig. 4 (b)). A broadening of the XMCD distribution up to 1 mT is observed matching the position of SAW peaks at $H_{\mathrm{lc,rc}}$. Upon further increasing the magnetic field the position of XCMD peak shifts to higher values, while the FWHM decreases, which corresponds to the gradual rotation of the CoFeB magnetization combined with erasing the domains completely.

THEORETICAL MODEL

To interpret the experimental results, we build a theoretical description of the SAW damping on the basis of Landau-Lifshitz-Gilbert equation, which allows us to reproduce the magneto-elastic sub-GHz SAW resonance in the exchange-spring magnet spin spirals of the IrMn-CoFeB heterostructure. Within this model, we associate the observed critical field, at which switching of the magnetization begins, with the in-plane magnetic anisotropy that has magneto-elastic origin. We assume that the spontaneous strains are formed at a saturation field and fix the direction of the strain-induced easy magnetic axis parallel to the external magnetic field $\mathbf{H}$. The strain-induced anisotropy does not change during the further field cycling and stabilizes metastable states with $\mathbf{M}$ ↑↓ $\mathbf{H}$ promoting a multidomain state within $H_{\mathrm{lc}} \leq H \leq H_{\mathrm{rc}}$ interval. The critical field $H_{\mathrm{lc,rc}}$, where the switching of magnetization begins, corresponds to the point at which the frequency of ferromagnetic resonance vanishes (see insets in Fig. 5). At these points the external magnetic field fully compensates anisotropy.

By minimizing the free energy of a ferromagnetic layer we calculate all possible equilibrium orientations of magnetization (parametrized by the angles φ_j in xy plane) as a function of the magnetic field for $\mathbf{H}\|\mathbf{H}_{\mathrm{EB}}$ and $\mathbf{H} \perp \mathbf{H}_{\mathrm{EB}}$ (see insets in Figs. 6 and 5). Remarkably, in both cases the magnetization has a nonzero projection on both x and y axes. In case $\mathbf{H}\|\mathbf{H}_{\mathrm{EB}}$ nonzero rotation of $\mathbf{M}$ from $\mathbf{H}$ direction is due to formation of the exchange spring within a ferromagnetic layer with a vertical length scale of at least five nanometers comparable to the escape depth of the photoelectrons contributing to the XMCD signal.
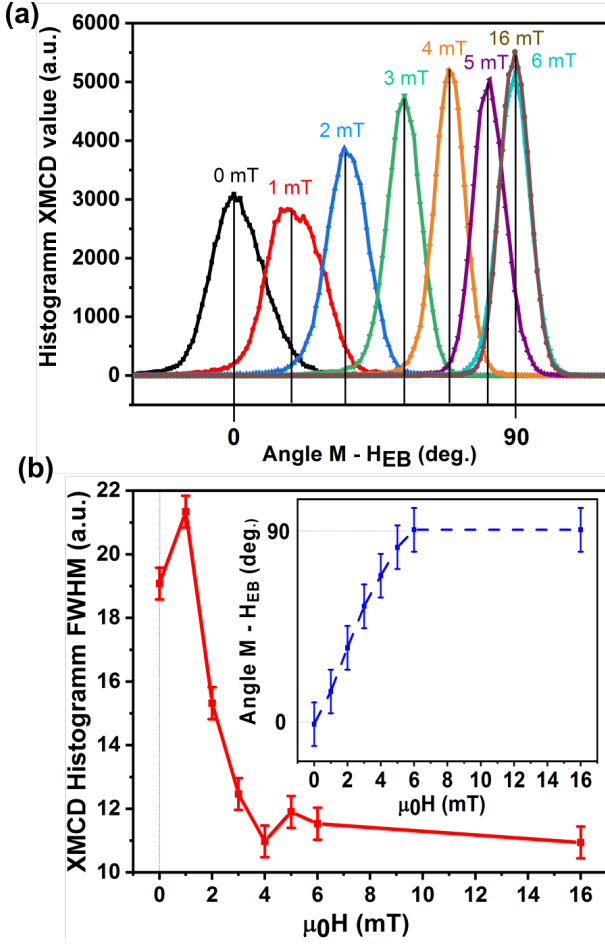
(a)

(b)

Figure 4. (Color online) Histogram of the XMCD distribution recorded at magnetic fields applied perpendicular to the exchange bias field ranging from 0 to 16 mT. The peak position represents the rotation angle of the net magnetization. (b) The FWHM analysis of the XMCD histograms reveals a maximal half width for an applied field of 1 mT, where also a maximal SAW damping value is observed for this geometry. The inset illustrates the gradual rotation of the CoFeB layer asymptotically approaching the saturation value of 90 angle degrees between the direction of the net magnetization M and the fixed direction of the exchange bias field H_{EB}.

Such a generic orientation of magnetization favours an efficient coupling of the longitudinal SAW with the magnetic system. Following Ref. [3] we calculate the field-dependence of SAW damping as a superposition of partial contributions from different magnetic domains (labeled by $j = 1, 2$):

$$\Delta S \propto P \propto \sum_j \frac{\xi_j \sin^2 2\varphi_j(H)}{\omega_{j\text{FMR}}^2(H) - \omega_{\text{SAW}}^2}, \qquad (1)$$

where P is the power density of ferromagnetic oscillations, ξ_j is a fraction of j-th domain, ω_{SAW}, ω_{FMR} are the angular frequencies of the incident SAW and ferromagnetic resonance and $\varphi_j(H)$ denotes the angle between k_{SAW} and M in the j-th domain, respectively.
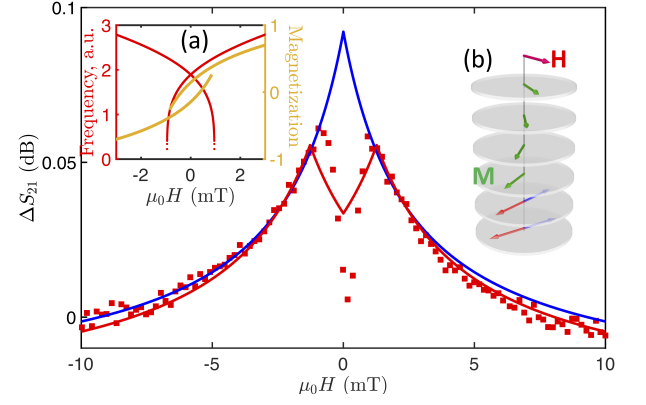

Figure 5. (Color online) Field dependence of the SAW $\Delta S_{21}(H)$ signal calculated from Eq. 1 (red solid line) assuming that $\xi_j \propto H$ while $H_{\text{lc}} \leq H \leq H_{\text{rc}}$ and $\mathbf{H} \perp \mathbf{H}_{\text{EB}}$. Experimental data is shown with red square dots. The blue line corresponds to the fitting of our model to the experimental data at large fields ($H \geq |H_{\text{lc}}|, H_{\text{rc}}$). The inset (a) on the left shows the calculated projection of magnetization on the field direction (orange line) and field dependence of $\omega_{j\text{FMR}}$ (red lines). The inset (b) on the right shows vertical distribution of $\mathbf{M}$ (green arrows) in the exchange spring pinned at the interface by the antiferromagnetic moments (red and blue arrows). The peaks in SAW amplitude can be associated with the frequency softening at the edges of bistability region.

Next, we note that in a single domain region, $H < H_{\text{lc}}$ or $H > H_{\text{rc}}$, the FMR frequency is much larger than the frequency of the SAW, $\omega(H) \gg \omega_{\text{SAW}}$ and $\omega(H) \propto \sqrt{H}$. Hence, as follows from Eq. (1), the field dependence of the damping amplitude should decay as $\Delta S \propto 1/(|H| + const)$, corresponding fitting is shown in Figs. 5, 6. On the contrary, in a bistablility region, $H_{\text{lc}} \leq H \leq H_{\text{rc}}$, ω_{FMR} critically decreases and vanishes at $H = H_{\text{lc}}$ and $H = H_{\text{rc}}$ (see inset in Fig. 5. In the vicinity of these points ΔS_{21} grows resonantly, corresponding to the peak valleys in the measured SAW signal of Figs. 5, 6).

The experimentally observed position of SAW peaks correlates well with the edges of stability extracted from magnetization data, we can associate the observed peaks in SAW amplitude with the frequency softening at the edges of bistability region. Since we expect that in the bistability region the sample is in a multidomain state so that both peaks (for parallel and antiparallel domains) are observed in each field run. According to our analysis, the magnetic response of the ferromagnet indicates the formation of partial domain walls (exchange springs) that mediate interaction between the magnetic and elastic subsystems. Importantly, we also believe that imperfections of the AFM/FM interface which usually define the value of the exchange bias field play an important role in the SAW attenuation mechanism. Even in the single domain regions these imperfections create local tilting of magnetization from x and y axes and enable coupling be-
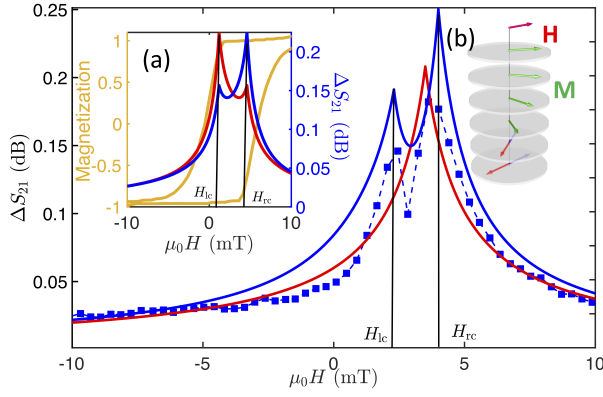
Figure 6. (Color online) Field dependence of the calculated SAW $\Delta S_{21}(H)$ signal (blue line) for $\mathbf{H} \| \mathbf{H}_{EB}$. The red line corresponds to fitting of the experimental data (points) at large fields ($H \geq |H_{lc}|, H_{rc}$). Inset (a): calculated SAW signal for increasing (blue) and decreasing (red) field scans. The domain fraction $\xi_j(H)$ is proportional to experimentally observed magnetization (orange line). Inset (b): vertical distribution of $\mathbf{M}$ in the exchange spring. In contrast to Fig. 5, the exchange spring spans both magnetic layers and involves the rotation of antiferromagnetic spins. One can observe that position of SAW peaks coincides with the stability points at which magnetization flips.
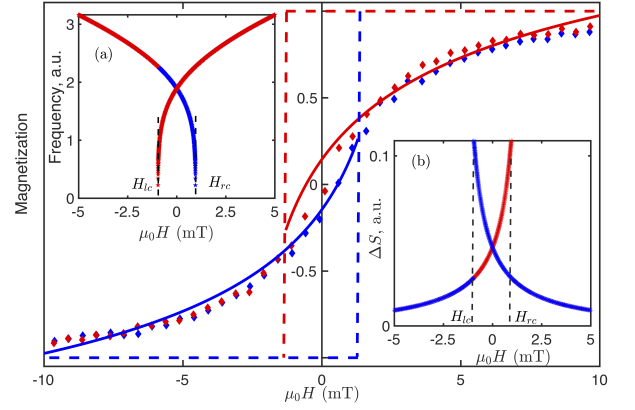

Figure 7. Magnetization component $m = M/M_s$ projected on the direction of the magnetic field $\mathbf{H} \perp \mathbf{H}_{EB}$ averaged over the thickness of a ferromagnetic layer. Diamonds correspond to experimental data, solid (dashed) lines are calculated for a single-domain state in an exchange biased (free) layer. Inset (a) shows field dependence of the FMR frequency (arbitrary units) in a single-domain state. Inset (b) shows the SAW damping from a single-domain state.

tween SAW and magnetization in a wide range of fields. We attribute the minimal discrepancy between our model and the experimentally observed SAW attenuation visible in Fig. 5 near zero field to an increased in-plane alignment in the direction of the established exchange bias field when approaching the FM-AFM interface in z-direction. Remarkably, our model matches the XMCD FWHM dependence on the magnetic field (Fig. 4 (b)) very well.

We consider the exchange bias as an interfacial field $\mathbf{H}_{EB}$ originating from the exchange coupling with an antiferromagnetic layer acting on the magnetization $\mathbf{M}$ of a ferromagnet in a small interfacial region $0 \leq z \leq \xi$. To obtain the equilibrium state of a ferromagnetic layer the free energy density, written as

$$F = -\frac{1}{2}M_s H_{an}^{\text{eff}}(\mathbf{m} \cdot \mathbf{u})^2 + 2M_s H_{an}^{\text{eff}} x_{\text{DW}}^2 \sum_{j=x,y} (\nabla m_j)^2 +$$

$$+\frac{1}{2}M_s H_{an\|} m_z^2 - M_s(\mathbf{H}_{\text{app}} \cdot \mathbf{m}) - M_s H_{EB}^{\text{loc}} \xi m_x \delta(z),$$
(2)

is minimized. Here $\delta(z)$ is the Dirac delta-function, M_s is saturation magnetization (per unit volume). The second term corresponds to the inhomogeneous exchange interaction within the CoFeB layer, x_{DW} is parametrizing the domain wall width. $H_{an\|} \gg H_{an}^{\text{eff}}$ denotes the out-of-plane anisotropy and H_{EB}^{loc} is the exchange coupling at the interface. The experimentally observed value of the exchange bias field is defined by averaging over the film

thickness, $\mathbf{H}_{EB} \approx H_{EB}^{\text{loc}} \xi/t_F$, where t_F is the film thickness. We assume that the in-plane domains of the CoFeB are rather large and solve the one-dimensional problem assuming exchange spring spirals present merely along the film normal (z axis).

We analyze the equilibrium states of the ferromagnetic layer starting from the experimentally obtained hysteresis loop shown in Fig. 7 (diamonds). In the case of the externally applied magnetic field $\mathbf{H}$ directed perpendicular to the exchange bias field $\mathbf{H}_{EB}$, the hysteresis loop is centered at $H = 0$ and shows a switching field of $H_c \approx 0.95$ mT. Upon applying the field anti-parallel to the exchange bias, $\mathbf{H} \| \mathbf{H}_{EB}$, the hysteretic loop exhibits a shift by 2.9 mT, as expected, with an coercitivity of 1.7 mT.

Assuming an in-plane anisotropy (parametrized with the effective field $H_{ms} > 0$) originating from spontaneous strains that stabilize the equilibrium orientation of the magnetization and introduce the coercitivity, the spontaneous strains once formed are fixed and do not change upon applying a magnetic field. Moreover, the direction of the strain-induced easy magnetic axis $\mathbf{u}$ depends on the initial state at large field ($|\mathbf{H}| \gg H_{an}^{\text{eff}}$) and is parallel to the external magnetic field $\mathbf{H}$.

Figure 7 shows the magnetization loops calculated for the $\mathbf{H} \perp \mathbf{H}_{EB}$ geometry assuming that $H_{an}^{\text{eff}} = 2.6$ mT.

Dashed lines correspond to homogeneous states in absence of the exchange coupling ($H_{EB} = 0$), with magnetization either parallel or anti-parallel to the external field.

The region in which two states with opposite direction of magnetization are stable is limited by the field values $H_{rc} = -H_{lc} = 0.95$ mT, at which the frequency of FMR

vanishes (dashed lines in inset (a)).

The solid line in Fig. 7 corresponds to the average projection of the magnetization on the direction of the magnetic field calculated from the Eq. 2 with $\xi = 1$ nm, $x_{DW} = 10$ nm, $H_{EB}^{loc} = 95.6$ mT, $t_F = 40$ nm, $\mathbf{H}_{EB} = 2.9$ mT.

The exchange spring equilibrium state in which the magnetization rotates from y axis (parallel or anti-parallel to $\mathbf{H}_{app}$) at the free surface of the ferromagnet toward x axis (parallel to $\mathbf{H}_{EB}$) at the antiferromagnet-ferromagnet interface. In the interval $H_{lc} \leq H_{app} \leq H_{rc}$ both exchange spring spirals with opposite orientations of $\mathbf{M}$ at the free surface are stable. By comparing the experimental and calculated magnetization curves we conclude that equilibrium state of the CoFeB corresponds to a single domain within the film plane incorporating an exchange spring spiral along the z axis.

In conclusion, in a joint experimental and theoretical approach, we have demonstrated that at ferromagnet-antiferromagnet interfaces, surface acoustic waves experience damping due to the pinning and formation of vertical exchange-spring spin spirals. Taking the IrMn-CoFeB magnetic thin film heterostructure as an example, we developed a quantitative model to microscopically understand the evolution of the vertical spin spirals and associated domain walls in CoFeB based on the Landau-Lifshitz equation reproducing our experimental SAW damping well for both geometries, i.e. $\mathbf{H} \| \mathbf{H}_{EB}$ and $\mathbf{H} \perp \mathbf{H}_{EB}$. As a result, we could associate the SAW damping maxima with the edges of a bistability region in the magnetization of CoFeB, where a pronounced magnetic field dependent drop in the FMR frequencies occur (FMR frequency softening). Our work shows that SAWs can prove very useful in probing complex magnetic structures possibly providing a new way to probe novel emergent non-collinear spin structures on-chip, which may prove indispensable in view of low energy-consumption spintronic devices.

ACKNOWLEDGEMENTS

---

* k.m.seemann@gmail.com

[1] M. Barangi, M. Erementchouck, P. Mazumder, J. Appl. Phys. **120**, 073901 (2016).

[2] R. F. Wiegert and M. Levy, IEEE Ultrasonics Symposium p. 311 (1988).

[3] M. Weiler, L. Dreher, H. Huebl, R. Gross, M.S. Brandt, and S.T.B Goennenwein, Phys. Rev. Lett. **106**, 117601 (2011).

[4] W. P. Robbins and A. Young, IEEE Transactions on Sonics and Ultrasonics **82**, 1539 (2010).

[5] W. P. Robbins and A. Hietala, IEEE Transactions on ultrasonics, ferroelectrics and frequency control **35**, 076402 (1988).

[6] D. Walikainen, R. F. Wiegert, and M. Levy, J. Appl. Phys. **63**, 3927 (1988).

[7] W. Edrington, U. Singh, M. A. Dominguez, J. Rehwaldt Alexander, R. Nepal, S. Adenwalla, Appl. Phys. Lett. **112**, 052402 (2018).

[8] M. Foerster, F. Macià, N. Statuto, S. Finizio, A. Hernández-Mínguez, S. Lendínez, P. V. Santos, J. Fontcuberta, J. M. Hernández, M. Kläui, and L. Aballe, Nat. Comm. **8**, 407 (2017).

[9] M. Foerster, L. Aballe, J. M. Hernández, and F. Macià, MRS Bulletin **43**, 854-859 (2018).

[10] B. Casals, N. Statuto, M. Foerster, A. Hernández-Mínguez, R. Cichelero, P. Manshausen, A. Mandziak, L. Aballe, J. M. Hernández, and F. Macià, Phys. Rev. Lett. **124**, 137202 (2020).

[11] E. E. Fullerton, J. S. Jiang, M. Grimsditch, C. H. Sowers, and, S. D. Bader, Phys. Rev. B **58**, 12193 (1998).

[12] F. Li, T. Nattermann, and V. L. Pokrovsky, Phys. Rev. Lett. **108**, 107203 (2012).

[13] S. Urazhdin, C. L. Chien, K. Y. Guslienko, and, L. Novozhilova, Phys. Rev. B **73**, 054416 (2006).

[14] M.-Y. Im, P. Fischer, K. Yamada, T. Sato, S. Kasai, Y. Nakatani, and T. Ono, Nature Comms. **3**, 983 (2012).

[15] Y. T. Chen and C. C. Chang, J. Alloys Compd. **498**, 113 (2010).

[16] C. Leighton, J. Nogués, B. J. Jönsson-Akerman, and, I. K. Schuller, Phys. Rev. Lett. **84**, 3466 (2000).

[17] E. Jiménez, J. Camarero, J. Sort, J. Nogués, N. Mikuszeit, J. M. García-Martín, A. Hoffmann, B. Dieny, and, R. Miranda, Phys. Rev. B **80**, 014415 (2009).

[18] J. Nogués and I. K. Schuller, J. Mag. Mag. Mater. **192**, 203 (1999).

[19] K. M. Seemann, F. Freimuth, H. Zhang, S. Blügel, Y. Mokrousov, D.E. Bürgler, and C.M. Schneider, Phys. Rev. Lett. **107**, 86603 (2011).

[22] M. ODonnell, E. T. Jaynes, and J. G. Miller, J. Acoust. Soc. Am. **69**, 696 (1981).

[21] S. Davis, A. Baruth, and S. Adenwalla, Appl. Phys. Lett. **97**, 232507 (2010).

[22] M. ODonnell, E. T. Jaynes, and J. G. Miller, J. Acoust. Soc. Am. **69**, 696 (1981).

[23] K. M. Seemann, F. Garcia-Sanchez, F. Kronast, J. Miguel, A. Kákay, C.M. Schneider, R. Hertel, F. Freimuth, Y. Mokrousov, and, S. Blügel, Phys. Rev. Lett. **108**, 77201 (2012).

[24] F. Kronast, J. Schlichting, F. Radu, Sh. Mishra, T. Noll, and, H.A. Dürr, Surf. Interface Analysis **42**, 1532 (2010).